Exp Fluids (2011) 50:1019–1030
DOI 10.1007/s00348-010-0988-8

RESEARCH ARTICLE

High-repetition-rate PIV investigations on a generic rocket model in sub- and supersonic flows

Martin Bitter · Sven Scharnowski · Rainer Hain · Christian J. Kähler

Received: 2 February 2010 / Revised: 10 September 2010 / Accepted: 25 September 2010 / Published online: 19 October 2010

Abstract High-repetition-rate PIV measurements were performed in the trisonic wind tunnel facility at the Bundeswehr University Munich in order to investigate the boundary layer parameters on a generic rocket model and the recirculation area in the wake of the model at Mach numbers up to Mach = 2.6. The data are required for the validation of unsteady flow simulations. Because of the limited run time of the blow-down wind tunnel, a high-repetition-rate PIV system was applied to obtain the flow statistics with high accuracy. The results demonstrate this method's potential to resolve small-scale flow phenomena over a wide field of view in a large Mach number range but also show its limitations for the investigations of wall-bounded flows.

1 Introduction

The transportation of satellites and other aero/astro-space technical equipment requires efficient delivery systems that fulfill a number of demands e.g. a high degree of reliability in extreme conditions comparable to those encountered in outer space, enough power to mobilize massive pieces of hardware and superior cost effectiveness. Reynolds-Averaged Navier–Stokes simulations (RANS) are well established to estimate the averaged flow field and predict payloads for low-cost aerodynamic designs of rockets. As unsteady effects play a dominant role, more sophisticated methods like URANS, LES and DES are required to characterize the flow dynamics and provide detailed diagnostics, necessary for a reliable prediction of the aerodynamic performance and structural loads. A large variety of recent numerical investigations using Reynolds-Averaged Navier–Stokes (RANS) methods (Lüdeke et al. 2006), large eddy simulations (LES) (Meiss and Schröder 2008) or detached eddy simulations (DES) (Deck et al. 2007) concentrate on the base flow of space vehicles.

However, with increasing capabilities of the numerical approaches, also unsteady experimental data are required to validate the flow simulations. This is why innovative and advanced measurement techniques must be developed and employed to overcome the limitations of current technology. Experimental data for the validation of the numerical results were gathered in several wind tunnel experiments. Herrin and Dutton (1994) performed pressure and LDV measurements up to Mach = 2.5 in order to characterize the average flow field in the wake of a rocket and the shear stresses produced by the unsteady vortex shedding. David and Radulovic (2005) carried out wind tunnel and in-flight measurements in order to examine the loads on the nozzle and the rear structure of the rocket caused by these unsteady vortices. In order to further investigate highly unsteady interactions, various blunt generic rocket configurations with and without exhaust plume simulation were examined. Several nozzle geometries that reflect the aerothermal loads in the base region of such a transportation system were designed, see Gülhan (2008). Investigations by Henckels et al. (2007) examined the impact of the exhaust plume on the pressure and density of the flow field in the aft body domain of the model for supersonic Mach numbers up to 11.2. Experiments carried out by van Oudheusden and Scarano (2008) analyzed the velocity flow field around the cylindrical base of the rocket model as well as the interactions of the free stream velocity field with the exhaust plume using particle image velocimetry (PIV) at

M. Bitter (✉) · S. Scharnowski · R. Hain · C. J. Kähler
Institute of Fluid Mechanics and Aerodynamics,
Universität der Bundeswehr München,
Werner–Heisenberg–Weg 39, 85577 Neubiberg, Germany
e-mail: martin.bitter@unibw.de

Mach number 3. The results of some of these investigations suggest the existence of highly unsteady pressure fluctuations with large amplitudes in the base region, which lead to strong mechanical loads on the rocket nozzle and could have damaging effects. Additionally, several close collaborations to perform numerical investigations and experiments have taken place in the recent years. The FESTIP (Future European Space Transportation Investigations Program) and the RESPACE project (Key Technologies for Reusable Space Systems) for example developed new technologies and new simulation methods for reusable launchers (see Pfeffer 1996; Gülhan 2008).

The work presented here is a sub-project of the SFB–TR 40 program, founded by the German research foundation (DFG). The scientific focus within the SFB–TR 40 is the analysis and modeling of coupled liquid rocket propulsion systems and their integration into the space transportation system (SFB/TR 40 2010). Based on reference experiments, numerical models are developed, which serve as a basis for efficient and reliable predictive simulation design tools. A combined optimization of the major components under high thermal and mechanical loads, e.g. combustion chamber, nozzle, structure cooling and aft body, is undertaken within the SFB–TR 40 program to achieve an enduring increase in the efficiency of the entire system.

In this contribution, the implementation and performance of PIV on a blunt generic rocket configuration will be presented in order to resolve the thin sub- and supersonic boundary and shear layers and to characterize the dynamics of the large-scale vortices in the wake flow domain up to Mach = 2.6. Only a high-resolution approach is capable of fulfilling the required demands to provide validation data for state-of-the-art numerical flow simulations due to the limited run time of the blow-down wind tunnel.

2 Setup and methodology

2.1 Wind tunnel facility

The measurements were performed in the Trisonic Wind tunnel Munich (TWM) at the Bundeswehr University, Munich. This facility is equipped with an independently adjustable Laval nozzle and diffuser, and it is therefore capable of generating sub-, trans- and supersonic flow. The TWM is a blow-down-type wind tunnel with two 30 m long storage vessels each with a volume of 190 m^3 (green in Fig. 1). Three air compressors with a total power of roughly 650 kW achieve a volume flow rate of 4,000 m^3/h. The compressed and dried air is stored in the two vessels at a maximum pressure of 20 bar. Less than 100 min are required for a complete filling.

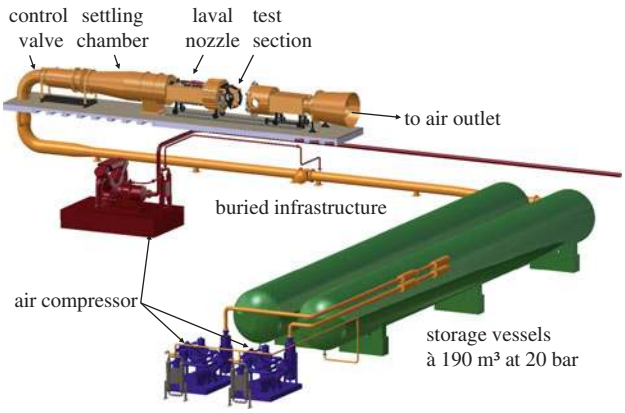

Fig. 1 Sketch of the Trisonic Wind tunnel Munich facility (TWM) at Bundeswehr University Munich

During wind tunnel operation, the pressure in the settling chamber is adjusted by the control valve in a closed-loop regime. While the pressure in the storage vessels drops continuously, the control valve is opened to compensate for the pressure losses. The pressure in the settling chamber is kept constant within 5 mbar tolerance. The total pressure range of this wind tunnel is $p_t = [1.2\cdots5]$ bar. This leads to a Reynolds number range of $Re = [7\cdots80] \times 10^6\ m^{-1}$. The settling chamber is several meters long and has a diverging cross section. Several flow straighteners are integrated in the settling chamber to reduce the turbulence level.

While the Reynolds number is controlled by the total pressure p_t, the Mach number is adjusted in the Laval nozzle, which is continuously deformable and has a rectangular cross section. A Mach number range between 0.3 and 3.0 can be obtained, with an accuracy of $\Delta Mach = 0.005$.

The 675 mm high, 300 mm wide and 1,200 mm long test section can be equipped with solid or slotted walls. The latter allows for boundary-layer suction. Both walls have round windows, 500 mm in diameter, for optical access to the test section. Additionally, the ceiling can be equipped with a 200 mm window if necessary.

Models can be mounted either on one of the walls or on a rear sting. In both cases, the angle of attack can be controlled by means of a hydraulic adjusting unit. The test section is surrounded by the plenum chamber, which can be opened pneumatically in order to get full access to the test section. An adjustable diffuser follows after the test section, and finally, the air leaves the wind tunnel through a tower outside the building (not shown in Fig. 1). The operating time of the TWM facility depends on the Reynolds and Mach number; it reaches up to 150 s at Mach = 3. The maximum flow rate (240 kg/s) is achieved at Mach = 1 and $p_t = 5$ bar, and the operating time is approximately 40 s at these conditions.

2.2 Generic rocket model

The tests were performed on a blunt axis-symmetric aluminum model with a polished base in order to minimize the laser light scattering at the wall, see Kähler et al. (2006). The configuration consists of a 36° cone with a spherical nose of $R = 5$ mm and a cylindrical part of $l = 164.3$ mm in length and a diameter of $ØD = 54$ mm. The total length of the model is $l = 231.3$ mm (see Fig. 2). A rear sting in the base of the cylinder was used for mounting the model in the test section to avoid the strong three-dimensional effects that a strut mounting would have on the flow and thus on the interactions in the base-flow regime (see van Oudheusden and Scarano 2008). This was done while being fully aware of the fact that a rear sting also influences the flow and possibly delays reattachment or causes an open wake. Hence, it is clearly a compromise but the best choice for the acquisition of reproducible validation data for numerical simulations. The diameter of the rear sting was chosen to be $Ød = 21.5$ mm so that it has the same dimensions of a later investigated nozzle for base-flow/plume interactions which is not presented in this contribution.

The Mach numbers used for the flow field investigations were selected according to specific stages of a real rocket launch: (a) shortly after the launch, (b) in the transonic region, (c) at hypersonic Mach numbers (Mach > 6, performed in other facilities). The lowest Mach number evaluated was Mach = 0.3 due to the wind tunnel limitations. The transonic range around Mach = 0.7 was of particular interest for the project partners as one of the objectives was to simulate the flow conditions shortly after the rocket launch, because at moderate heights, the ambient conditions (air pressure and density) cause strong flow/structure interactions that could lead to high mechanical stresses in the involved components. Additional Mach numbers, Mach = 2.0 and Mach = 2.6, were also evaluated to close the gap between the transonic data and some already existing data at hypersonic Mach numbers. All relevant test parameters are tabulated in Table 1.

Three flow domains of major interest along the model were chosen for the investigations, see Fig. 2. Setup 1 was chosen in order to investigate the ability of the tracer particles to follow the motion of the flow at the junction between the cone and the cylindrical part as well as to quantify the state of the boundary layer (laminar/turbulent). The fields of view (FOV) for setup 2 and 3 were selected in order to determine the velocity profiles just before the base of the model as well as the Reynolds shear stresses and flow topology in the wake. These profiles are essential for comparison with the unsteady flow simulations (e.g. as the wake structure depends on the boundary layer parameters).

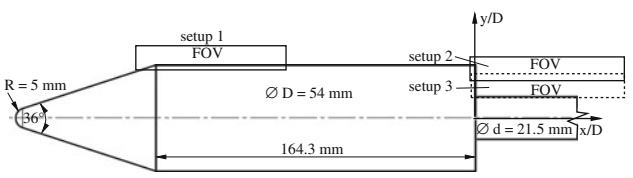

Fig. 2 Sketch of the generic rocket model for the wind tunnel measurements. The three fields of view (FOV) from major interest in the conducted PIV investigations are outlined

Table 1 Test parameters for the PIV investigations for boundary layer and wake flow characteristics

Setup	1	2	3
Mach	0.3; 0.7; 2.0; 2.6		
Re_D (10^6)	0.7; 1.0; 2.2; 1.7		
p_t (bar)	2.0; 1.5; 3.2; 3.2		
FOV W × H (mm^2)	125 × 20	125 × 40	125 × 26
Pixel array (px^2)	1,280 × 200	1,280 × 400	1,280 × 250
Magnification M	1:5		
Δt (μs)	6; 3; 1.5; 1.5		10; 5; 3; 3
Recordings N	10,000	5,000	8,000
Rate f_{Acq} (Hz)	500	2,000	4,000

The FOV varied between 125 mm^W × 20 mm^H and 125 mm^W × 40 mm^H according to the investigations. Details can also be found in Table 1.

2.3 PIV setup

Due to the limited run time of the facility and the large number of recordings required for the estimation reliable statistical data, a high-repetition-PIV system using a *Quantronix* Darwin Duo Nd:YLF double-pulse laser with a pulse duration of $t_p \approx 120$ ns and a laser energy of 22 mJ per cavity at 1 kHz was used. The laser beam is transformed into a light sheet using two spherical lenses with focal lengths of −40 mm and +50 mm for adjusting the height of the light sheet, followed by two cylindrical lenses with focal lengths of −25 mm and +50 mm for width adjusting, see Fig. 3.

Due to density differences between the pressurized plenum chamber and the laboratory, where the PIV components are installed, a perpendicular access of the laser beam into the plenum chamber was necessary to avoid refractions caused by density changes during the wind tunnel run. Otherwise, pressure differences between the inside and the outside of the test section would lead to spatial misalignment of the laser light sheet during the wind tunnel run and hence a dislocation of the region of interest. Finally, a mirror (#2 in Fig. 3) located in the rear sting mounting redirects the beam to illuminate the investigated field of view. A spring mechanism which is

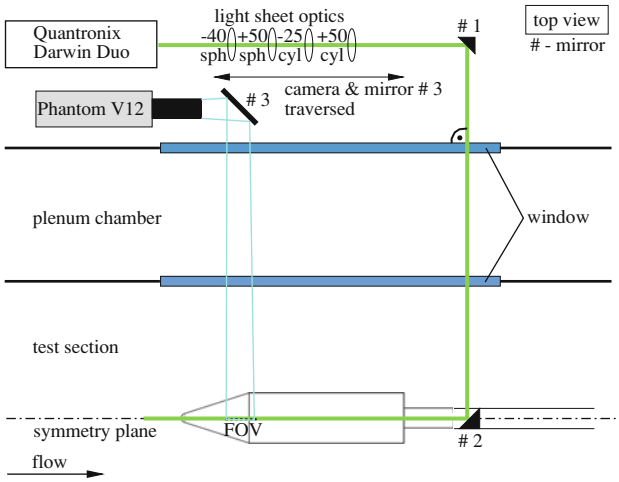

Fig. 3 Sketch of the experimental setup for the PIV investigations in the Trisonic Wind tunnel Munich (TWM). The dimensions are not scaled

locked during the experiment allows for slight horizontal and vertical adjustments of about ±2° to cover the fields of view. The solid connection of the mirror with the rear sting mounting damps its vibrations and suppresses the relative motion of the laser sheet with respect to the model.

The M^2 factor of the laser was estimated to $M^2 \approx 25$, which led to a light sheet thickness in the focal line of $s_1 \approx 1{,}500$ µm for the chosen setup. This relatively thick light sheet was assumed to still be suitable for these investigations due to the expected two-dimensional flow behavior on the cone and the large scale of the wake structure.

The recordings were captured using a *Phantom* V12 high-repetition-rate CMOS camera with a 1,280 × 800 px^2 sensor and 8 GB of internal memory. At full resolution, a maximum recording rate of about 6,200 images/s was achievable, which led to 3,100 PIV double-frame images per second. In order to increase the recording rate, the sensor size was cropped, see Table 1. The time between the laser pulses was adjusted according to Table 1, between $\Delta t = 1.5$ µs for the supersonic Mach numbers and $\Delta t = 6$ µs for Mach = 0.3, in order to restrict the particle displacement to 10 pixel. The lowest interframing time allowed by the CMOS camera is $\Delta t = 0.5$ µs. A *Zeiss* Sonnar T* AE 2.8/180 mm objective lens with an f-number of 4 was connected to the camera. The particle image diameter was about 2–3 px for this optical setup.

2.4 Frequency analysis of the wind tunnel setup

The major motivation for the preliminary investigations in this section is the analysis of the near-wall turbulent boundary layer domain. Therefore, the vertical vibration of the model during a wind tunnel run was analyzed in order to qualify the region where reliable information of the boundary layer topology could still be obtained.

The vibrations appearing in the PIV recordings are a superposition of vibrations from the model, the wind tunnel and the camera system. This section analyzes in detail the appearing motion of the generic rocket model and of the wind tunnel itself during an experiment in order to separate their interactions with one another with respect to the excitation of dominant frequencies or significant model motion.

As the model is mounted by a steel-made rear sting in the wind tunnel, it is moving due to bending of the rear sting during the experiment. To determine the motion, two markers (0.5 mm in diameter), one at the wall of the wind tunnel and one at the beginning of the cylindrical part of the model, were tracked during a wind tunnel run using a *Phantom* V12 CMOS high-speed camera at a sampling frequency of 10 kHz. A normalized cross-correlation of each recorded (and inverted) image with a reference image taken while the model was stagnant gives the time response of the motion from which the frequency amplitude is computed. Since the scene is measured in the *x*/*z*–plane, only the vertical motion was captured. Figure 4 shows the spectral amplitude of the vertical motion of the marker for Mach = 0.7 at $\mathrm{Re_D} = 1.0 \times 10^6$. For these settings, the load is the largest for the case considered in this investigation.

The orange curve in Fig. 4 illustrates the motion of the wind tunnel with respect to the camera. No distinct peaks appear in this spectrum. The standard deviation of this

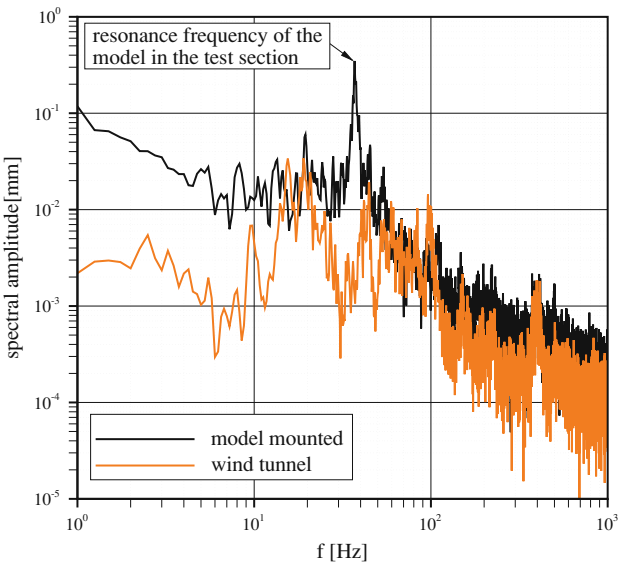

Fig. 4 Frequency spectrum versus the spectral vertical amplitude captured for the wind tunnel without the model (*gray*) and the generic rocket model in the test section (*black*) during a wind tunnel run at Mach = 0.7

motion is 70 μm in the vertical direction. Hence, the vibration of the wind tunnel creates a negligible random motion in the PIV recordings.

There is a significant maximum at a frequency of $f = 38$ Hz during the run with the mounted model in the test section. This is related to the resonance frequency of the model, which was determined by exciting the model with a single impulse from its resting state. The maximum corresponds to an amplitude in the angle of attack of $\Delta\alpha = \pm 0.1°$. Other Mach and Reynolds numbers have been tested and showed similar spectra. The amplitudes of the vibrations are proportional to the Reynolds number. Furthermore, it is highest for Mach numbers close to one.

It is clearly shown that the vibration of the PIV system caused by the vibration of the flow while the wind tunnel is running is negligible compared to the motion of the model inside the wind tunnel. The frequency of vortex shedding in the base region is expected to be around $f = 400$ Hz for Mach $= 0.3$ and around $f = 850$ Hz for Mach $= 0.7$, based on a Strouhal number of $St_D = 0.2$ according to Geurts (2006). In order to correct the model vibration in the PIV recordings, a shift correction algorithm is applied for a reliable evaluation of the near-wall regions of the boundary layer in setup 1 and also for the characterization of the wake flow in setup 2 and 3. Details of this procedure are outlined in Sect. 2.7.

2.5 Numerical analysis of the particle tracking behavior

In order to investigate the ability of seeding particles of different diameters to follow the curved stream lines in the flow around the rocket model, numerical computations by means of the commercially available CFD tool Fluent V12 were performed and will be discussed in this section. The aim is to simultaneously estimate the sizes of particles that are able to follow the fluid faithfully in the diverted flow regions and those which remain in the boundary layer. The fully turbulent computations were performed in 2D and 3D. In order to concentrate on the particle tracking in the plane of the field of view, the 3D results are not regarded here. Strong asymmetric three-dimensional flow effects, caused by the non-squared dimensions of the test section, had an influence on the particle trajectories and led to this decision. The Reynolds stress model was used to close the equations. The scaled residuals were evaluated during the computation (residual limit: 1e-5), and a converged solution was reached after approximately 15,000 iterations.

This approach allows for the injection of inert spherical particles of different diameters at the vicinity of the model's nose and for the tracking of their 2D trajectories. This gives an impression of how seeding particles of varying diameters follow the flow in accelerated and decelerated regions close to the wall. Therefore, the physical and thermodynamic properties of the DEHS seeding fluid (e.g. density or viscosity) were fed into the tool. Seeding particles of $ØD = [0.5;1;2]$ μm in diameter were introduced into the flow field at $x/D = -4.6$ at different y-positions: at the center-line ($y/D = -0.5$), at $y/D = -0.44$ (middle) and at $y/D = -0.39$ (high). The results of the investigations are shown in Fig. 5 for Mach $= 0.7$ and in Fig. 6 for Mach $= 2.0$. The colored trajectories represent the injected DEHS particles of the different diameters. The different line types show their positions relative to the center line of

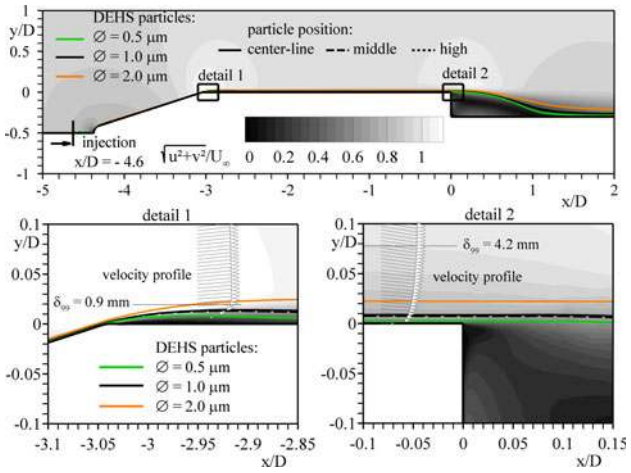

Fig. 5 Results of the numerical simulations to investigate the influence of particle diameter on its diversion at Mach $= 0.7$ for three different particle diameters (colored trajectories) at different positions (*line types*). *top*: normalized velocity magnitude in the vicinity of the model, *bottom left*: close-up at the kink between cone and cylinder, *bottom right*: close-up of the model base

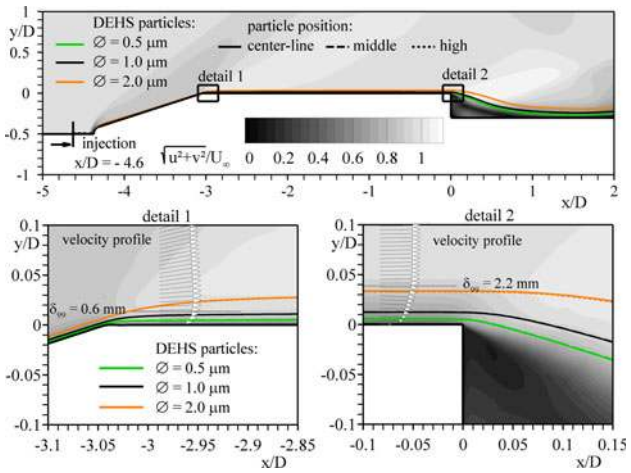

Fig. 6 Results of the numerical simulations to investigate the influence of particle diameter on its diversion at Mach $= 2.0$ for three different particle diameters (colored trajectories) at different positions (*line types*). *top*: normalized velocity magnitude in the vicinity of the model, *bottom left*: close-up at the kink between cone and cylinder, *bottom right*: close-up of the model base

the flow field. The detail images show a close-up of the particle diversion on the change from cone to cylinder and at the base of the model. This computational approach can give hints to estimate the particle sizes which follow the flow and thus allow us to resolve it in the near-wall regions of the boundary layer.

Additionally, a boundary layer profile in these regions is shown, which is extracted from the computations in order to get an impression of the velocity profile's topology at the appropriate case. The data from the simulations is compared to data derived from the experiments in Sect. 3.1.

It must be clearly stated, again, that the shown trajectories are derived from two-dimensional steady-state computations. As turbulent fluctuations in the boundary layer cause a mixing of particles present close to the model, it is possible to observe particles closer to the wall as predicted by the simulations. Unsteady shedding vortices in the wake will also capture particles so that there is a certain particle concentration in the recirculation area.

The position where the particles are injected is not from major importance. The lines for center line, middle and high injected particles lie almost on top of each other.

It is clearly visible that the particle concentration in the region of the model base strongly depends on the diameter of the particles. The smaller the particles are, the higher their probability of following the strong diversion at the kink between the cone at the nose and the cylindrical part of the body. With particles of 0.5 or 1 μm in diameter, it is possible to resolve the flow down to the near-wall regions of the boundary layer. The 2 μm particles already seem to have too much inertia to follow the gradients in the flow. At the kink, the 2 μm particles are already transported outside the boundary layer, so that a resolution of the near-wall flow region is hardly possible for both simulated Mach numbers. An agglomeration of the 2 μm particles at nearly the same wall distance can be detected no matter where they were injected. Hence, it can be conducted that a near-wall boundary layer resolution is only possible with particles that are 1 μm in diameter or smaller.

2.6 Seeding

As described in the previous section, only tracer particles with diameters smaller than 1 micrometer are suitable for these experiments. Contrariwise, the larger the particles, the higher the scattered-light intensity, which determines the signal-to-noise ratio of the PIV recordings. Hence, a particle size of 1 μm is a trade-off between sufficient scattered-light intensity and good response to high velocity gradients in the flow. In the present study, the tracer particles were generated from DEHS (Di-Ethyl-Hexyl-Sebacat) by using two *PivTec* seeding atomizers, which fulfill the requirements regarding the particle-size distribution. Seeding particles with a mean diameter of 1 μm and a relaxation time of about 2 μs are produced by this kind of atomizer, see Kähler et al. (2002), PivTec (2010) and Ragni et al. (2010).

For observing small-scale flow phenomena with PIV, a large tracer-particle concentration is required due to the large magnification, see Kähler et al. (2006) as well as Kähler and Scholz (2006). Therefore, the seeding atomizers are equipped with 40 and 45 nozzles, respectively.

During the wind tunnel run, the particle size was controlled by the pressure difference within the nozzles of the particle generators. A difference of 1 bar between the settling chamber and the pressure just before the nozzles was found to be the optimum (Kähler et al. 2002). The particles were injected into the settling chamber right after the position of the control valve, see Fig. 1. This not only ensures a homogeneous distribution of the particles in the flow but also leads to a low turbulence level just before the test section. A local seeding in a downstream position would always disturb the flow significantly.

2.7 Image processing techniques

An image preprocessing was applied to the acquired data:

- Only PIV recordings with a homogeneous seeding concentration were selected. The particle density in the test section is not constant due to pressure and density differences with changing Mach number and inadequate mixing based on heavy pressure fluctuations behind the control valve.
- The correlation peak was enhanced by filtering CMOS background noise and reflections in the PIV images.
- Vertical model movements were corrected for a reliable PIV evaluation down to near-wall regions.

In order to select PIV images with a sufficient seeding concentration, a simple particle count algorithm implemented in the evaluation software *DaVis* by LaVision was used. A rectangle with 10 $mm^W \times 10\ mm^H$ was considered in the corresponding field of view, and images with a seeding density of more than 10 particle images were chosen for further evaluation purposes. The vertical model movement was corrected using a multi-pass cross-correlation algorithm written in *Matlab*. The motion of two characteristic regions of an image sequence (e.g. reflections) was calculated relative to the first image of the series. The two intensity profiles of the appropriate regions were extracted from the first image and detected in the subsequent ones using a multi-pass cross-correlation approach with a window size of $64^2\ px^2$ in the initial run. In a second run, a cross-correlation was performed between the first image of the series and the shift-corrected images from run 1. If the remaining shift amplitude exceeded a threshold of more than 0.3 px, the

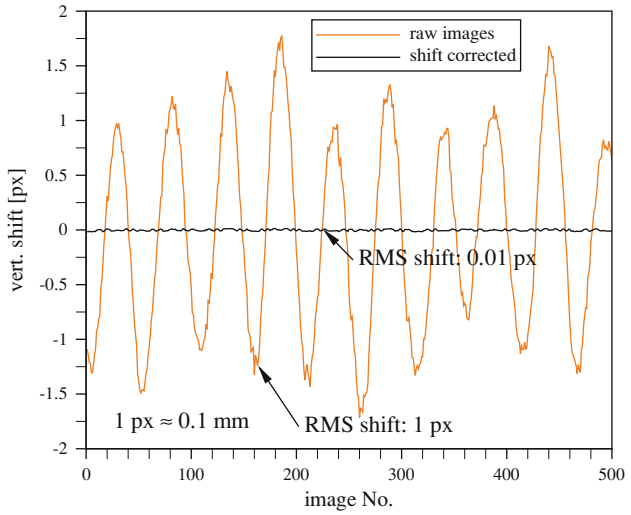

Fig. 7 Exemplary application of the shift correction algorithm to 500 raw images recorded at Mach = 0.7. The *orange curve* shows the model vertical amplitude during the wind tunnel run, and the *black curve* represents the shift-corrected results

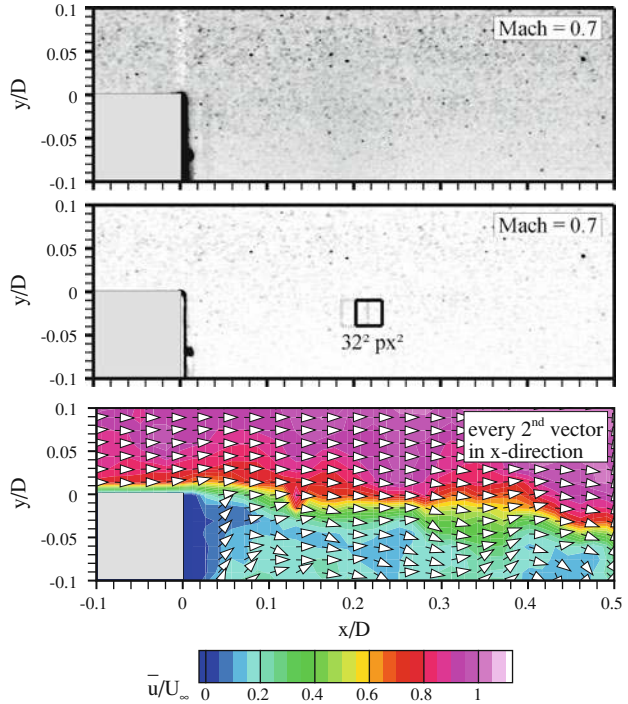

Fig. 8 Clipping of an inverted raw PIV recording for Mach = 0.7 in the vicinity of the base (*top*). Intensity-filtered and shift corrected image for further PIV evaluation (*middle*). Detail of an instantaneous velocity field in the vicinity of the base, every second vector is shown in*x*-direction (*bottom*)

images were not included in the further PIV evaluation. In Fig. 7, the vertical motion for the first 500 images of a raw image series at Mach = 0.7 is exemplarily shown (orange curve) as well as the remaining image shift after the initial shift correction pass (black curve). The shift correction calculation was made with the raw, non-filtered images but was applied to the filtered images. For the final evaluation process, about 90% of the original captured number of recordings could be used. A PIV evaluation of the raw images led to a large number of spurious vectors due to background reflections caused by the polished walls of the test section. Therefore, an additional filtering procedure was performed on the PIV images. In order to filter the raw images, a local average over the time series was calculated. The spatial filtering diameter of 5^2 px^2, which is slightly larger than a particle image, was used. The average value was subtracted from every single recording.

In Fig. 8 an inverted raw PIV recording (top), a filtered and shift-corrected (middle) and an instantaneous velocity field (bottom) for Mach = 0.7 demonstrates the image preprocessing potential discussed above. Due to display effects, it seems that the number of seeding particles is reduced from step one to step two. However, the effective signal-to-noise ratio is increased by this procedure.

3 PIV results

3.1 Boundary layer investigations

In this section, the results of the boundary layer investigations in the deflection region are presented for Mach = [0.3; 0.7; 2.0]. The number of recordings for each case is about 10,000 images, as outlined in Table 1. The field of view was 125 mm^{W} × 20 mm^{H}, whereas only the first 76 mm (or $x/D = 1.5$ respectively) are shown here in order to preserve clarity in the figures.

The normalized absolute velocity fields derived from the measurements are plotted in Fig. 9. The three figures visualize the evaluation of the boundary layer height (δ_{99}) with increasing extent in the x-direction. The data were calculated using a multi-pass sum-of-correlation algorithm with a decreasing correlation window size from 12^2 px^2 to 6^2 px^2, 50% overlap, and a Gaussian window weighting with a 4:1 stretching in x-direction, (Kähler et al. 2006). The image preprocessing algorithm discussed above was applied.

At the kink located at $x/D = 0$, a laser reflection from the model's surface impeded the evaluation. Unfortunately, the reflection extends up to $x/D \approx 0.3$ at Mach = 0.7, so that a separation bubble predicted by the numerical simulations could not be resolved in the experiments.

The extracted velocity profiles at distinct x-positions show the development and change of the boundary layer topology with increasing Mach and Reynolds numbers. Every fifth vector of the velocity profile is shown in the wall-normal direction.

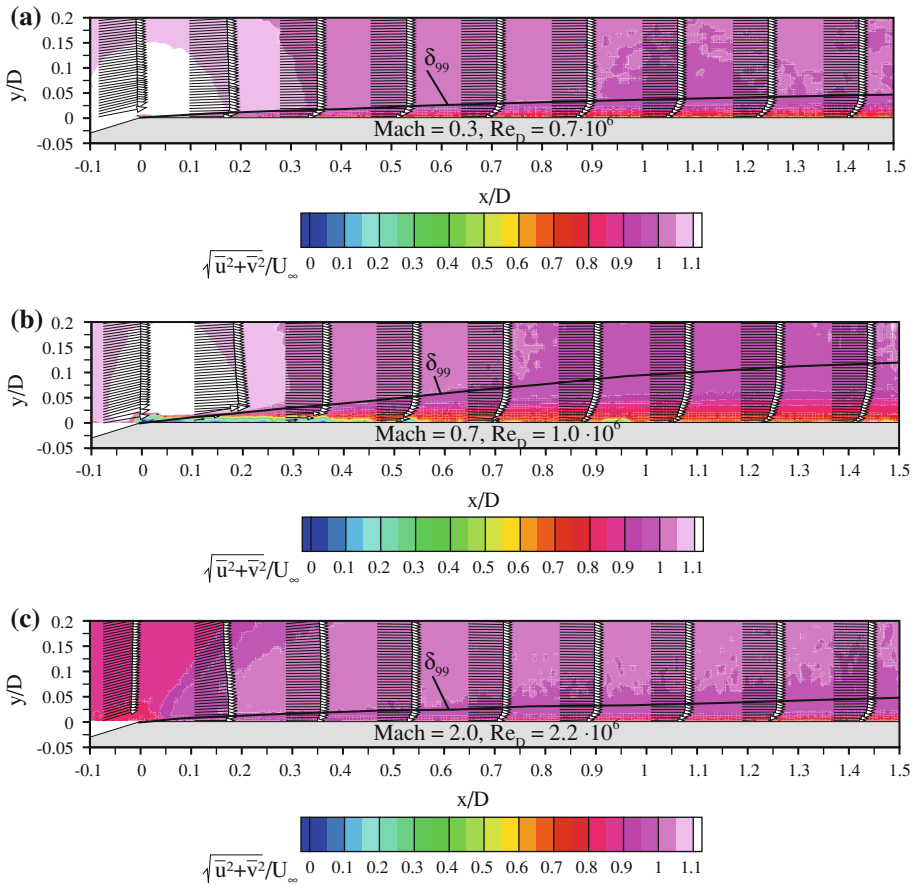

Fig. 9 Development of the boundary layer topology for **a** Mach = 0.3, **b** Mach = 0.7 and **c** Mach = 2.0. The absolute mean velocity is color-coded. Velocity profiles at certain positions were extracted from the data to visualize the growth of the boundary layer height δ_{99} across the surface

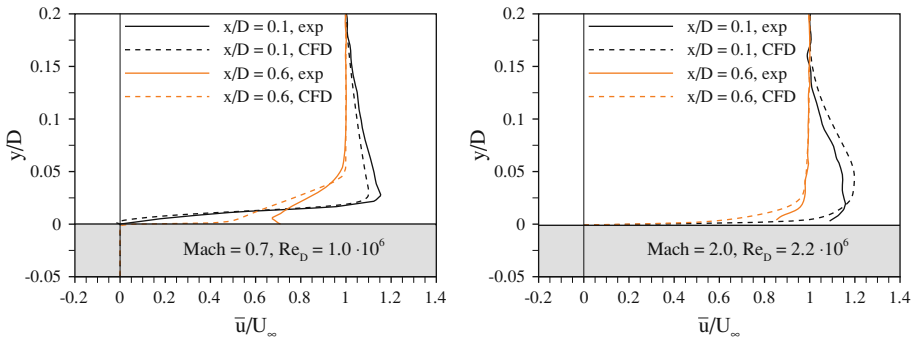

Fig. 10 Comparison of the boundary layer profile for Mach = 0.7 (*left*) and Mach = 2.0 (*right*) at $x/D = 0.1$ (*black*) and $x/D = 0.6$ (*orange*) between experimental and numerical data. The experimental data are outlined by the *solid lines*, and the simulated data are shown by the *dashed lines*

The boundary layer profile in all three cases implies a fully turbulent flow state shortly after the kink position. Nevertheless, the low thickness of the boundary layer also reveals the challenging goal of resolving the near-wall gradients in the flow, which is a necessary step for the validation of numerical models. In Fig. 10, two velocity profiles at $x/D = 0.1$ (black) and $x/D = 0.6$ (orange), extracted from the PIV data (solid) and from the numerical calculations (dashed), are shown for Mach = 0.7 and Mach = 2.0. The entire boundary layer height at $x/D = 0.6$ was resolved with 45 structured cells and a stretching of 1.15:1 in the numerical simulations. In the PIV results, the entire boundary layer height was resolved within 25 pixel.

The final correlation window size of 6^2 px^2, with a 50% overlap, led to only ≈ 12 boundary layer sampling points in the wall-normal direction at $x/D = 0.6$. In the vicinity of the wall, the PIV evaluation causes errors mainly based on: (a) the size of the final correlation window, (b) a reduced seeding particle concentration and (c) the remaining uncertainties in the exact determination of the wall based on the exact knowledge of the laser light sheet position.

Due to these reasons, no evaluation of the boundary layer profile down to the wall is possible. The velocity profiles derived from the measurements seemed to have a slightly more turbulent character compared to the simulated ones. The gradients in the logarithmic parts agree

well at $x/D = 0.1$, whereas a systematic difference can be seen at $x/D = 0.6$ for both Mach numbers. In order to resolve the logarithmic region and the decay of the streamwise velocity component to zero at the wall, in this experiment, the magnification of the imaging system must be increased by a factor of 20 in order to resolve the viscous sub-layer region with at least 4–5 pixels. Therefore, a long-range micro-PIV technique with single-pixel-resolution evaluation would fulfill the demands if particles appear in this region (Kähler et al. 2006). Nevertheless, the comparison of the experimental and the numerical data indicates the capability of the setup to characterize the boundary layer statistics.

3.2 Wake flow characterization

Finally, the results of the PIV measurements in the wake of the rocket model at setup position 2 and 3 are presented. The results for three Mach numbers, Mach = [0.7; 2.0; 2.6], at Reynolds numbers between $Re_D = [1.0–2.2] \times 10^6$ are discussed. Note, however, that the case of Mach = 0.7 is the most interesting one for the project because of the high aerodynamic loads on the nozzle.

For each case, between 5,000 and 8,000 double-frame images were acquired with up to 4 kHz, see Table 1. An overlapping field of view of 125 $mm^W \times 55$ mm^H was investigated. This leads to an axial wake resolution of roughly two model diameters behind the rocket.

The time delay between the laser pulses for the investigations of the shear layer and outer flow regime was nearly halved compared to the one used for the characterization of the recirculation domain, compare Table 1. The image preprocessing discussed in Section 2.7 was again applied to the raw data. The evaluation was performed using the LaVision DaVis software. As a first step for the vector field computation, a second-order multi-pass sum-of-correlation algorithm with decreasing window size down to 16^2 px^2 pixel and 50% overlap was used to calculate the initial average velocity field. This vector field was used as a starting solution for the final vector field calculation by means of a normalized multi-pass cross-correlation algorithm with decreasing correlation window size down to 16^2 px^2 and 50% overlap at Mach = 0.7 and down to 32^2 px^2 and 50% overlap at the supersonic Mach numbers due to a lower seeding density. Finally, a post-processing algorithm, including median filtering, where outliers were eliminated by a correlation peak ratio threshold of 1.3 (ratio of highest peak minus global minimum to second highest peak minus global minimum), was applied. Near-wall regions were masked due to a less reliable computation of the velocity vectors caused by laser light reflections which led to self-correlation of the reflections.

Plots of subsonic flow at Mach = 0.7 and two supersonic flows at Mach = 2.0 and Mach = 2.6 are shown in Figs. 11, 12 and 13. The corresponding upper plots show the absolute normalized velocity field in the wake behind the model, and the lower plots represent the distribution of the Reynolds shear stresses.

As a general overview, it can be stated that it is feasible to characterize the spatial extension of the recirculation domain in the wake with the chosen PIV setup even at supersonic

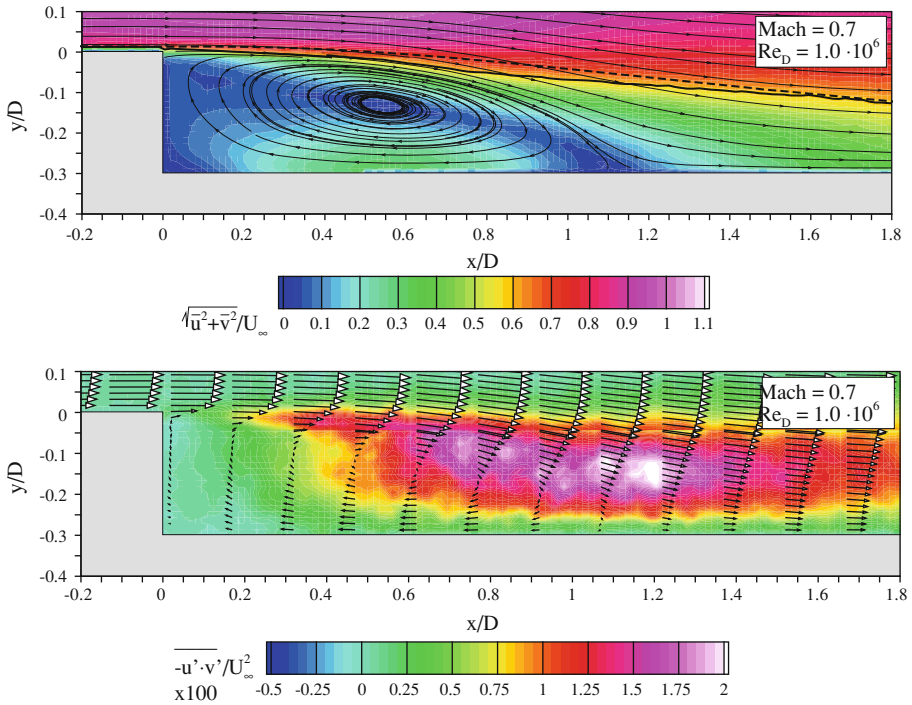

Fig. 11 Normalized mean velocity magnitude (*top*) and Reynolds stresses (*bottom*) in the wake region for Mach = 0.7 at $Re_D = 1.0 \times 10^6$

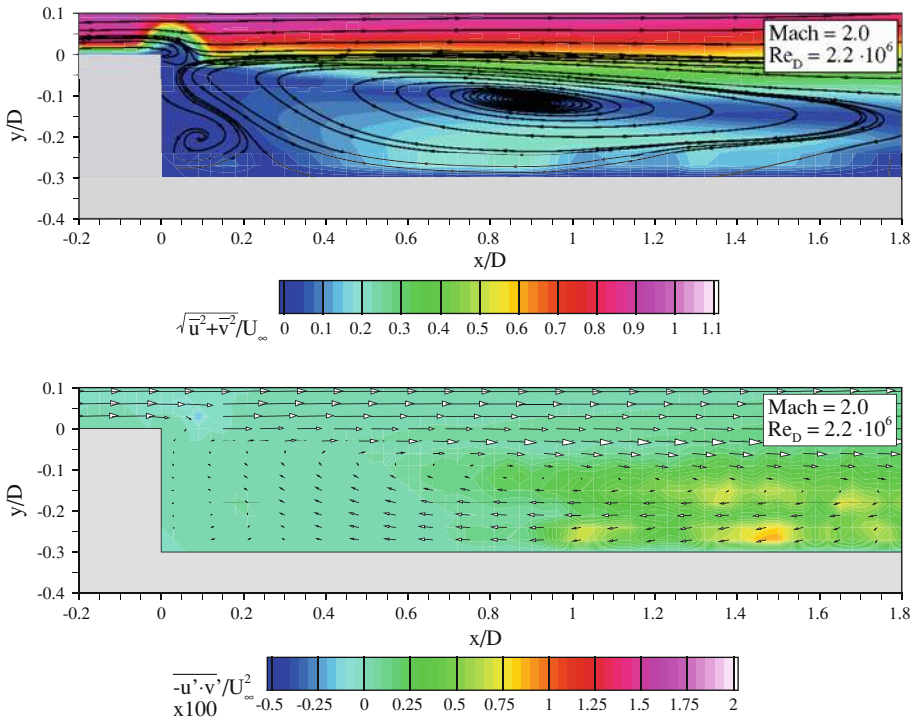

Fig. 12 Normalized mean velocity magnitude (*top*) and Reynolds stresses (*bottom*) in the wake region for Mach = 2.0 at $Re_D = 2.2 \times 10^6$

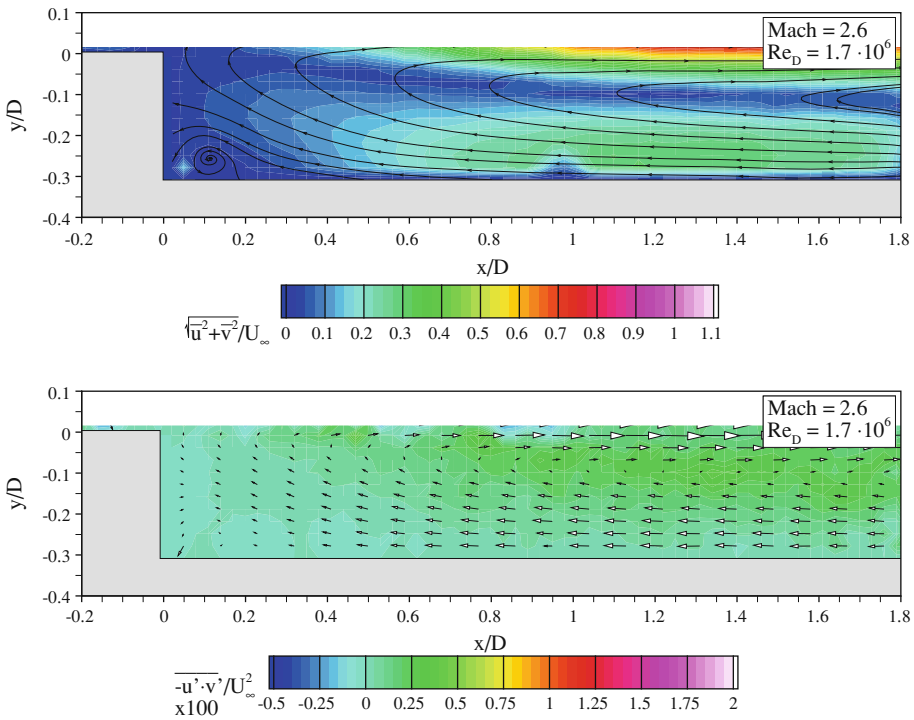

Fig. 13 Normalized mean velocity magnitude (*top*) and Reynolds stresses (*bottom*) in the wake region for Mach = 2.6 at $Re_D = 1.7 \times 10^6$

Mach numbers. A distinct recirculation area with a clear reattachment location develops for Mach = 0.7. The dark solid line in Fig. 11 represents the path of the separation stream line between the inner recirculation domain and the outer flow extracted from the PIV data. On the other hand, the dark dashed line represents the numerical computations. The criteria for the separation stream line were the constant ratio Φ_s between the axial velocity of the outer flow U_e and the axial velocity of the mixing zone u_m given by

$$\Phi_s = \frac{u_m}{U_e} = 0.597, \quad (1)$$

initially proposed by Chapman (1986) and adapted by Tanner (2003). The results reveal a good agreement

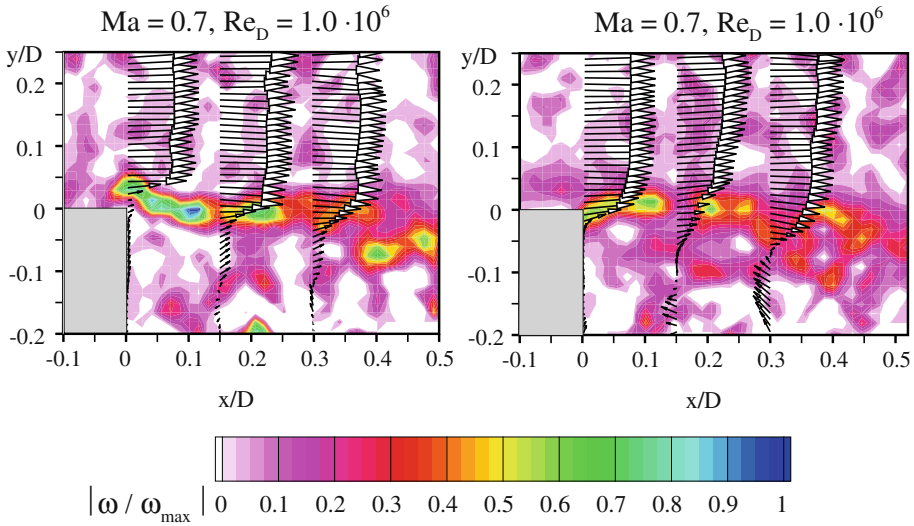

Fig. 14 Subsequent instantaneous normalized vorticity distribution for Mach = 0.7. The normalization value was $|\omega_{max}| = 250{,}000$ 1/s

between the two-dimensional computations and the experiments with respect to the volume and the spatial extent of the recirculation area. Regarding the shear layer, a strong turbulence amplification is indicated by the Reynolds stresses.

A broadening of the shear layer toward the reattachment point indicates unsteady fluctuations of the reattachment point and a strong momentum transfer between the outer free stream flow and the wake flow caused by vortex shedding at the base.

In the case of the supersonic Mach numbers, the recirculation area spreads far away from the model base, which suggests the assumption of an open wake. The reasons for this, which include: (a) the rear sting mounting, (b) the strut, to which the rear sting is clamped, or (c) the mirror for the laser beam, have not been fully examined yet.

Problems with an inadequate light sheet, caused by the destruction of the mirror from particle impacts, prevented an evaluation of the flow field for y/D larger than 0.02 for Mach = 2.6. No distinct development of the shear layer could be shown for this case.

Finally, the rapid spatial growth of the shear layer and its dynamics were analyzed. For the case of Mach = 0.7, two subsequent instantaneous vorticity distributions are shown in Fig. 14. The vorticity field is normalized with the maximum vorticity in the flow field ($|\omega_{max}| = 250{,}000$ 1/s). The shedding of vortices is indicated by the velocity vectors at the three x/D-positions. The high amplitude of the spatial change of the shear layer explains the strong widening of the Reynolds shear stresses in the wake for Mach = 0.7.

Figure 15 exemplarily shows the spectral amplitude of the horizontal velocity component of a fixed point in the wake of the model for Mach = 0.3. The position was selected so that the average streamwise velocity equals zero and the coordinates were $x/D = 0.75$, $y/D = -0.15$.

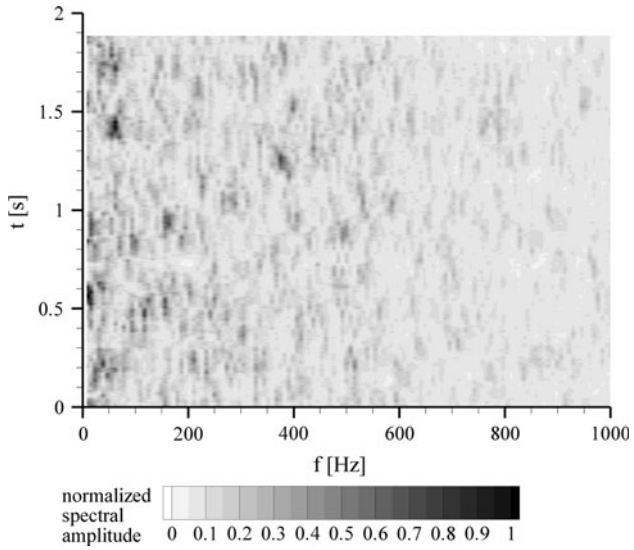

Fig. 15 Temporal development of the spectral amplitude for the Mach = 0.3 case

A total of 8,000 PIV recordings acquired at 4 kHz were analyzed. The flow in the wake appears to be highly unsteady. It does not show periodic behavior over a longer time. In order to extract more information from the signal, the analysis was performed in the following way: The time series was chopped in small pieces consisting of 512 time steps before computing the spectrum. The starting point was shifted continuously with the intention to analyze the temporal development of the spectral amplitude. Figure 15 shows the results for each time step as a 2D plot. In order to compute the amplitudes at $t = 0.5$ s in this figure, a Fourier transformation of the period $t = 0.5-0.628$ s was performed.

Overall, it is visible that the amplitude is fairly low for frequencies higher than 600 Hz. However, several dark areas

can be seen below that. They correspond to a high amplitude of a certain frequency at a certain time. But none of them appear for a longer interval, which means that a single dominant vortex shedding frequency does not exist. Only short-term periodic structures with varying dominant frequencies are observed in the wake flow.

4 Conclusions and outlook

The results show the capabilities of high-repetition-rate PIV to resolve boundary layers and large-scale wake structures in sub- and supersonic flows.

The results reveal in combination with numerical investigations that only seeding particles smaller than 1 micrometer in diameter (based on DEHS particles) are suitable for the characterization of the near-wall region and dynamic structures in the wake.

For a reliable estimation of the velocity profiles and flow statistics down to the near-wall region, the vibration of the model in the wind tunnel and the facility itself was analyzed. For a high-accuracy evaluation of the boundary layer topology, even these small movements are valuable to be taken into account. A shift correction algorithm with subpixel accuracy is proposed. With this approach, the boundary layer topology estimated from the high-repetition-rate PIV experiments showed a good agreement with the numerical simulations.

The logarithmic region of the boundary layer could not be resolved with the chosen experimental setup. Therefore, a long-range microscopic PIV approach in combination with a single-pixel evaluation is recommended to achieve the desired resolution in the vicinity of the wall for the validation of numerical simulations. The characterization of the shedding vortices in the wake and the quantification of the Reynolds stresses in the shear layer could be measured at all Mach numbers. The temporal analysis of the wake's frequency spectrum showed no existence of periodic vortex shedding. Only the presence of small coherent vortex packages could be proved. It is confirmed that high dynamic loads caused by unsteady shedding vortices could interact with the nozzle (here: the sting) and could lead to structural damaging.

Acknowledgments Financial support from the German Research Foundation(Deutsche Forschungsgemeinschaft—DFG) in the framework of the Sonderforschungsbereich Transregio 40 is gratefully acknowledged by the authors.

References

Chapman GT (1986) Topological classification of flow separation on three-dimensional bodies. In: 24th AIAA, Aerospace Sciences Meeting, Reno, NV, USA, p 22

David C, Radulovic S (2005) Prediction of buffet loads on the ariane 5 afterbody. In: 6th international symposium on launcher technologies, Munich, Germany

Deck S, Thepot R, Thorigny P (2007) Zonal detached eddy simulation of flow induced unsteady side-loads over launcher configurations. In: 2nd European conference for aerospace sciences, Brussels, Belgium

Geurts E (2006) Steady and unsteady pressure measurements on the rear section of various configurations of the ariane 5 launch vehicle. Technical report NLR-TP-2006-596, National Aerospace Laboratory NLR

Gülhan A (ed) (2008) RESPACE—key technologies for reusable space systems, notes on numerical fluid mechanichs and multidisciplinary design, vol. 98. Springer, Berlin Heidelberg

Henckels A, Gülhan A, Neeb D (2007) An experimental study on the base flow plume interaction of booster configurations. In: 1st CEAS European air and space conference, Berlin, Germany

Herrin JL, Dutton J (1994) Supersonic base flow experiments in the near wake of a cylindrical afterbody. AIAA J 32(1):77–83

Kähler CJ, Scholz U (2006) Transonic jet analysis using long-distance micro-PIV. In: 12th international symposium on flow visualization—ISFV 12, Göttingen, Germany

Kähler CJ, Sammler B, Kompenhans J (2002) Generation and control of particle size distributions for optical velocity measurement techniques in fluid mechanics. Exp Fluids 33:736–742

Kähler CJ, Scholz U, Ortmanns J (2006) Wall-shear-stress and near-wall turbulence measurements up to single pixel resolution by means of long-distance micro-PIV. Exp Fluids 41:327–341

Lüdeke H, Calvo JB, Filimon A (2006) Fluid structure interaction at the ariane-5 nozzle section by advanced turbulence models. In: European conference on computational fluid dynamics—ECCOMAS CFD. TU Delft, The Netherlands

Meiss JH, Schröder W (2008) Large-eddy simulation of the base flow of a cylindrical space vehicle configuration. In: 6th European symposium on aerothermodynamics for space vehicles, Versailles, France

Pfeffer H (1996) Towards reusable launchers—a widening perspective. Tech. rep., European Space Agency—ESA

PivTec (2010) URL http://www.pivtec.com

Ragni D, Schrijer F, van Oudheusden BW, Scarano F (2010) Particle tracer response across shocks measured by PIV. Exp Fluids. doi: 10.1007/s00348-010-0892-2

SFB/TR 40 (2010) URL http://www.sfbtr40.de

Tanner M (2003) A theory for incompressible two-dimensional steady base flow with application to two different problems. Aerosp Sci Technol 7:340–351

van Oudheusden BW, Scarano F (2008) Chap PIV investigation of supersonic base-flow-plume interaction. In: Topics in applied physics, vol 112. Springer, Berlin / Heidelberg, pp 465–474